Towards multiscale modelling of complex liquids using hybrid particle-continuum schemes

R. Delgado-Buscalioni,[1, *] P. V. Coveney,[2, †] and G. De Fabritiis[3, ‡]

¹Depto. Física Teorica de la Materia Condensada,
Universidad Autónoma de Madrid, Campus de Cantoblanco, Madrid, E-28049, Spain.
²Centre for Computational Science, Department of Chemistry,
University College London, 20 Gordon Street, WC1H 0AJ London, U.K.
³Computational Biochemistry and Biophysics Laboratory (GRIB), Universitat Pompeu Fabra,
Barcelona Biomedical Research Park (PRBB), C/ Dr. Aiguader 88, 08003, Barcelona, Spain
(Dated: April 16, 2008)

Due to the interplay between molecular and mesoscopic processes, the modelling and simulation of complex liquids at nano and micron scales require a multiscale approach. We propose a hybrid technique designed to handle multiscale phenomena, which retains the full molecular nature of the system where it is of interest while coarse-graining it elsewhere. The method couples molecular dynamics (MD) and fluctuating hydrodynamics (FH) based on the Landau theory. Mean flows involving transport of transversal (shear) and longitudinal momentum (sound) are coupled across the interface of both MD and FH domains. Hydrodynamic fluctuations of mass and momentum are transferred, preserving consistency with hydrodynamics and thermodynamics. Here we illustrate the hybrid method by studying the reflection of water sound waves against a lipid (dimyristoylphosphatidylcholine, DMPC) monolayer.

Keywords: Multiscale modelling, nanofluidics, molecular dynamics, fluctuating hydrodynamics, lipid membranes

I. INTRODUCTION

Fluid dynamics at the nanoscale is attracting considerable attention due to the possibility of building nano and microscopic devices to process small quantities of products, a common scenario in contemporary biotechnology. These devices use flows to transport and mix materials. However, the dimension of the channels is so small that fluid-boundary interactions may need to be taken into account at the molecular level. Furthermore, the nanoscale does not always permit a simple Navier-Stokes (NS) description, due to the presence of thermodynamic fluctuations which become apparent at this scale. Because of this, it is useful to use Landau's fluctuating hydrodynamics equations which generalize the NS equations to small scales by adding a random term to represent the stress tensor fluctuations [1, 2]. In this paper, using a hybrid computational technique based on coupling molecular dynamics and fluid dynamics, we study the response of a lipid monolayer subjected to sound waves in water [3]. In so doing, we demonstrate that the hybrid MD method is able to reproduce similar results to purely molecular approach, while a fluid dynamics solver would fail to reproduce the interaction of the sound waves with the molecular boundary. In the following, we present in sections II and III a brief summary of the coupled model hybrid MD and its main components, molecular dynamics and Landau's fluctuating hydrodynamics. In section

IV, we present our results for waves reflected by a lipid monolayer and finally, in section V, we draw some conclusions.

II. MESOSCOPIC AND MOLECULAR DESCRIPTIONS

A. Fluctuating hydrodynamics level

Hydrodynamics at micron scales is described by the fluctuating hydrodynamic (FH) equations [2, 4]. These are stochastic partial differential equations which reduce to the Navier-Stokes equations in the limit of large volumes. Fluctuating hydrodynamics is based on conservation equations of the form $\partial_t \phi(\mathbf{r}, t) = -\boldsymbol{\nabla} \cdot \mathbf{J}^\phi$, where ϕ is the density of any conserved quantity (mass, momentum, energy) and $\boldsymbol{J}^\phi$ is the flux of the conserved quantity. As in Ref. [1] we restrict ourselves to an isothermal fluid for which the conserved quantities are mass and momentum, with densities $\rho(\mathbf{r}, t)$ and $\boldsymbol{g}(\mathbf{r}, t)$ respectively. Mass and momentum fluxes are

$$\boldsymbol{J}^\rho = \boldsymbol{g}\boldsymbol{v}, \tag{1}$$

$$\boldsymbol{J}^{\boldsymbol{g}} = \left(\boldsymbol{g}\boldsymbol{v} + \boldsymbol{\Pi} + \widetilde{\boldsymbol{\Pi}}\right), \tag{2}$$

where the velocity field $\boldsymbol{v}$ satisfies $\boldsymbol{g} = \rho\boldsymbol{v}$ and $\boldsymbol{J}^\rho$, $\boldsymbol{J}^{\boldsymbol{g}}$ are the mass flux vector and the pressure tensor respectively. The pressure tensor in Eq. (2) contains the convection term $\boldsymbol{g}\boldsymbol{v}$ and the stress tensor, divided into deterministic (mean) and fluctuating parts, $\boldsymbol{\Pi}(\mathbf{r}, t)$ and $\widetilde{\boldsymbol{\Pi}}(\mathbf{r}, t)$, respectively. The deterministic part of the stress tensor

---

*rafael.delgado@uam.es
†p.v.coveney@ucl.ac.uk
‡gianni.defabritiis@upf.edu

corresponds to that of a Newtonian fluid

$$\mathbf{\Pi} = (p + \pi)\mathbf{1} + \overline{\overline{\mathbf{\Pi}}}^S, \qquad (3)$$

where p is the equilibrium thermodynamic pressure given by the equation of state while the trace and traceless symmetric part of the stress tensor are, respectively,

$$\pi = -\zeta\partial_\gamma v_\gamma \qquad (4)$$

$$\overline{\Pi}^S_{\alpha\beta} = -\eta\left(\partial_\alpha v_\beta + \partial_\beta v_\alpha - \frac{2}{3}\partial_\gamma v_\gamma \delta_{\alpha\beta}\right), \qquad (5)$$

where the convention of summation over repeated indexes is used. The shear and bulk viscosities are η and ζ respectively. The fluctuating stress tensor $\widetilde{\Pi}_{\alpha\beta}$ appearing in Eq. (2) is a random Gaussian matrix with zero mean which is delta correlated in space and time. We refer to Refs.[1, 2] for the explicit form of the correlation function.

For the sake of completeness we include the discrete form of the FH equations obtained from the finite volume method [1]. These equations provide the change of mass dM^t_k and momentum $d\boldsymbol{P}^t_k$ in cell k at time t,

$$dM^t_k = \sum_l \boldsymbol{g}_{kl} \cdot \boldsymbol{e}_{kl} A_{kl} dt, \qquad (6)$$

$$d\boldsymbol{P}^t_k = \sum_l \left\{ \boldsymbol{v}_{kl}\mathbf{g}_{kl} + \frac{(p_l + \pi_l) + \overline{\overline{\mathbf{\Pi}}}^S_l}{2} \right\} \cdot \mathbf{e}_{kl} A_{kl} dt \quad (7)$$
$$+ d\widetilde{\mathbf{P}}^t_k$$

where V_k is the volume of cell k, $\boldsymbol{e}_{kl}$ is the unit vector perpendicular to the contact surface of area A_{kl} from volume k to volume l (in our regular lattice $A_{kl} = A$ is fixed). Note that the summations in Eqs. (6) and (7) are performed over all the $\{l\}$ control cells that are in contact with cell k. The discrete versions of the pressure tensor components introduced in Eqs. (4) and (5) read

$$\pi_k = \frac{\zeta}{V_k} \sum_l \frac{A_{kl}}{2} e^\beta_{kl} v^\beta_l, \qquad (8)$$

$$\left[\overline{\overline{\mathbf{\Pi}}}^S_k\right]_{\alpha\beta} = \frac{\eta}{V_k} \sum_l \left[\frac{A_{kl}}{2}(e^\alpha_{kl} v^\beta_l + e^\beta_{kl} v^\alpha_l) - \frac{\delta^{\alpha\beta}}{D} A_{kl} e^\gamma_{kl} v^\gamma_l \right].$$

Finally, as shown in Refs. [5, 6] the momentum contribution of the fluctuating stress can be evaluated from

$$d\widetilde{\boldsymbol{P}}^t_k = \sum_l \frac{A_{kl}}{2}\sqrt{4k_B T \frac{\eta}{V_l}} d\overline{\mathbf{W}}^S_l \cdot \mathbf{e}_{kl}$$
$$+ \sum_l \frac{A_{kl}}{2}\sqrt{2Dk_B T \frac{\zeta}{V_l}}\frac{tr[d\mathbf{W}_l]}{D}\mathbf{e}_{kl}, \qquad (9)$$

where $d\mathbf{W}_l$ is a $D \times D$ matrix ($D = 3$ in three dimensions) of independent Wiener increments satisfying $\langle d\mathbf{W}^{\alpha,\beta}_k d\mathbf{W}^{\gamma,\delta}_l \rangle = \delta_{k,l}\delta_{\alpha,\gamma}\delta_{\beta,\delta} dt$ and $d\overline{\mathbf{W}}^S_l$ is a traceless symmetric random matrix defined as

$$d\overline{\mathbf{W}}^S_l = \frac{(d\mathbf{W}_l + d\mathbf{W}^T_l)}{2} - \frac{tr[d\mathbf{W}_l]}{D}\mathbf{1}. \qquad (10)$$

For details on the imposition of boundary conditions for the density and momentum we refer to Refs. [1, 7].

B. Molecular dynamics level

The molecular description is based on classical molecular dynamics. We use the CHARMM27 forcefield incorporating the TIP3P parametrization, which specifies bond, angle, dihedral and improper bonded interactions and non-bonded Lennard-Jones 6-12 and Coulomb interactions. The code is derived from a stripped down version of NAMD [8]. In the molecular domain we use a dissipative particle dynamics (DPD) thermostat [9] to preserve local momentum conservation and thus hydrodynamic modes.
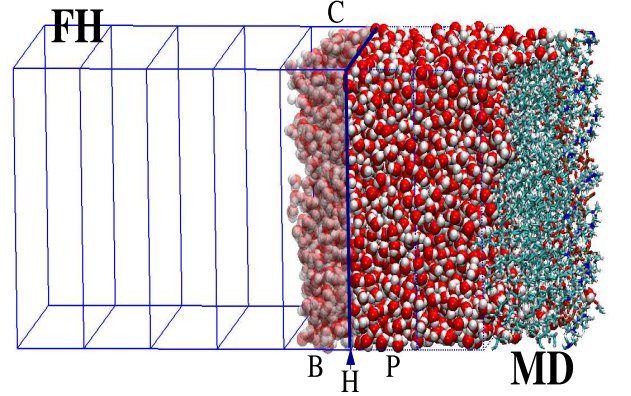
III. COUPLING METHOD

FIG. 1: Geometry of the domain decomposition used in the present hybrid calculations. Fluctuating hydrodynamics (FH) and molecular dynamics (MD) domains are separated by the *hybrid* interface H. The particle buffer is B. Finite volume control cells adjacent to the H interface are labelled as C and P. The MD domain is composed of water interfacing a lipid monolayer formed by DMPC.

In our computational implementation, the MD and FH components are independent *coupled models* [10] which exchange information after every fixed time interval Δt_c. We set $\Delta t_c = n_{FH}\Delta t = n_{MD}\delta t$, where Δt and δt are the FH and MD time steps and, n_{FH} and n_{MD} are integers which depend on the system being modeled. For water as solvent $\Delta t_c = 100$ fs, $n_{FH} = 10$ and $n_{MD} = 100$. Conservation is based on the flux balance: both domains receive equal but opposite mass and momentum fluxes across the hybrid interface. This interface, H, (see Fig. 1) uniquely defines the total system, formed by MD+FH. This is important because it permits one to clearly evaluate the overall mass and momentum of the system. By contrast, in previous schemes [11] particle and continuum

domains intertwine within a larger overlapping region, thus preventing a clear definition of the system.

As shown in Fig. 1, the whole simulation volume is divided into non-overlapping *control cells* which are used in the finite volume method for solving the fluid dynamics equations. In Fig. 1 we illustrate the control cells adjacent to the interface H. These cells are called C and P to indicate that they are located on the *continuum* and *particle* sides of H, respectively. The region B in Fig. 1 is the particle buffer, which is part of the particle region (MD+B) (but not part of the overall system which, as stated, is MD+FH). The buffer B is in fact used as a particle *reservoir* to impose momentum on the MD domain.

The central quantity within our scheme is the flux of momentum across H because mass flux across H arises *as a consequence* of the momentum flux [12]. This approach is consistent with fluid dynamics and avoids the spurious extra imposition of mass across H.

A. Evaluation of the momentum flux across H

Using the approximation made by the finite volume method, the momentum flux across H is

$$\boldsymbol{J}_H^{\boldsymbol{g}} \cdot \boldsymbol{e}_\perp = \frac{\boldsymbol{J}_P^{\boldsymbol{g}} + \boldsymbol{J}_C^{\boldsymbol{g}}}{2} \cdot \boldsymbol{e}_\perp. \tag{11}$$

where $\boldsymbol{J}_C^{\boldsymbol{g}}$ and $\boldsymbol{J}_P^{\boldsymbol{g}}$ are the momentum fluxes at the adjacent C and P cells, respectively. According to the vector $\boldsymbol{e}_\perp$ normal to the hybrid interface, Eq.(11) provides the flux of momentum across H towards the P cell. For conservation, the flux imposed towards C should be $-\boldsymbol{J}_H^{\boldsymbol{g}}$.

We now explain how to obtain $\boldsymbol{J}_C^{\boldsymbol{g}}$ and $\boldsymbol{J}_P^{\boldsymbol{g}}$. The C cell belongs to the FH domain so $\boldsymbol{J}_C^{\boldsymbol{g}}$ is directly obtained from Eq. (2). Note, however, that the velocity gradient appearing in the local mean stress $\boldsymbol{\Pi}_C$ in Eq. (8), for k =C, requires the local density and velocity of the neighbouring l =P cell of the MD domain. These quantities, ρ_P and $\boldsymbol{v}_P$, are obtained from the instantaneous mass and momentum at P

$$M_P = \sum_{i \in P} m_i \tag{12}$$

$$\boldsymbol{P}_P = \sum_{i \in P} m_i \boldsymbol{v}_i, \tag{13}$$

where the summation runs over those molecules within the P cell. The local density and velocity are $\rho_P = M_P/V_P$ and $\boldsymbol{v}_P = \boldsymbol{P}_P/M_P$ respectively.

The momentum flux tensor at P, $\boldsymbol{J}_P^{\boldsymbol{g}}$, can be evaluated using either a microscopic or a mesoscopic approach. The microscopic approach uses the Irving-Kirkwood formula,

$$\boldsymbol{J}_P^{\boldsymbol{g}} = \frac{1}{V_P} \langle \sum_{i \in P} m_i \mathbf{v}_i \mathbf{v}_i + \mathbf{W}_i \rangle_{[\delta t_s, \Delta t_c]}, \tag{14}$$

where $\mathbf{W}_i = (1/2) \sum_{j \in P} \mathbf{r}_{ij} \cdot \mathbf{f}_{ij}$ is the contribution of atom i to the virial part of the stress tensor [13]. In the most general case, $\boldsymbol{J}_P^{\boldsymbol{g}}$ and $\boldsymbol{J}_C^{\boldsymbol{g}}$ are time averaged over the coupling time Δt_c (see Ref. [1] for details).

Alternatively, the "mesoscopic" route to calculate $\boldsymbol{J}_P^{\boldsymbol{g}}$ uses the local coarse-grained variables at l =P and neighbouring cells to feed Eqs. (2) and (8). The fluctuating part of momentum flux tensor is treated similarly to the other FH cells (Eq. 9).

B. Flux boundary conditions

To guarantee momentum conservation after each coupling time Δt_c we need to introduce $\boldsymbol{J}_H^{\boldsymbol{g}} \cdot \boldsymbol{e}_\perp \Delta t_c$ momentum into the MD domain and the opposite of this into the FH domain. This momentum flux can be inserted into the FH domain using standard techniques for the finite volume scheme [1, 7]. In our formulation one only needs the pressure tensor $\boldsymbol{J}^{\boldsymbol{g}}$ at neighboring cells to update the momentum in Eq. (7). In particular, for k =C, one just needs $\boldsymbol{J}_P^{\boldsymbol{g}}$ from the MD system to close the system of equations for FH cells.

By contrast, the imposition of the desired momentum flux into the MD system is one of the more delicate parts of the coupling scheme. This task is equivalent to imposing an external force $\mathbf{F}_H$ which introduces the desired input of momentum ($A \boldsymbol{J}_H^{\boldsymbol{g}} \cdot \boldsymbol{e}_\perp \Delta t_c$) into the MD region over the coupling time. To impose this external force we use the particle buffer B (see Fig. 1). Particles are free to enter or leave this buffer across H, but once inside B, each particle $i \in B$ feels an external force $\mathbf{f}_i^{ex}$. The total external force is set to $\sum_{i \in B} \mathbf{f}_i^{ex} = \mathbf{F}_H$, so that the exact amount of pressure and stress is transferred to the *whole* particle system, MD+B.

With each buffer particle acting as a momentum carrier which transfers a part of the force from the outer region, it is important to ensure that there are enough momentum carriers sharing the external force. This issue is solved by controlling the number of particles in B, N_B. We use $\Delta N_B = (\langle N_B \rangle - N_B) \Delta t / \tau_B$ where $\langle N_B \rangle$ is set proportional to the mass at the overlapping C cell. Molecules leaving the buffer cell are simply removed and, if $\Delta N_B > 0$, then new molecules are placed in B with a velocity taken from the Maxwellian distribution and $\langle \boldsymbol{v} \rangle = \mathbf{v}_C$, where $\mathbf{v}_C$ is the velocity in the C cell. The insertion location is determined by the USHER algorithm [14, 15], which efficiently finds new molecule configurations, releasing an energy equal to the mean energy per molecule.

Finally, in order to preserve momentum conservation, momentum exchange due to molecule insertion/removal should be taken into account in the overall momentum balance. We simply calculate the amount of momentum due to particle insertion/removal and correct the external force to ensure that over the coupling time, it exactly introduces a momentum equal to $A \boldsymbol{J}_H^{\boldsymbol{g}} \cdot \boldsymbol{e}_\perp \Delta t_c$. This issue is discussed in detail in Ref. [12].

The reader may be already aware that we are imposing the external momentum on the *entire* particle sys-

tem (MD+B) and that this does not ensure the desired amount of momentum crossing the interface H towards the MD domain. Indeed, as a consequence, we do not conserve the momentum of the overall system (MD+FH), but rather that of MD+FH+B. The error in momentum conservation, however, is a small quantity, bounded by the finite size of the buffer B. As shown in Ref. [3], after few hundreds of femtoseconds the accumulated errors in momentum conservation becomes smaller than the standard deviation of momentum in one cell due to thermal fluctuations. A slight modification in the coupling scheme enabling *exact* momentum conservation has been presented in Ref. [16].

An important feature of the present scheme is that the mass flux across the hybrid interface H is not imposed, but arises naturally from the pressure gradient and convection across the interface. Over the coupling time Δt_c, the mass flowing towards C across H is obtained simply by counting the number of molecules crossing the interface. This amount of mass, ΔM_H^{MD}, is injected into the adjacent C cell of the FH model, so that mass is conserved. To transfer this mass into the C cell we use a relaxation equation which injects the mass crossing the MD domain [1, 3].

The water density profile within the buffer region is similar to those observed in liquid-vapor coexistence (see [3] and [17]); the rarefied region being near the buffer end. As explained in Ref [16] we ensure that the density profile is flat around the hybrid interface H. This avoids any spurious current induced by density gradients and it also ensures that the orientation of water molecules within the MD domain is that of bulk water. In fact, as shown by Chacón *et al.* [17] the orientation of water dipoles is only altered at the outermost layer, adjacent to the rarefied region.

IV. WATER SOUND WAVES PROPAGATING AGAINST A LIPID MONOLAYER

The problem of reflection of water sound waves colliding against lipid monolayers was introduced in Ref. [3] as a non-trivial test case for the hybrid MD scheme. The setup is shown in Fig. 1; each lipid molecule is tethered by the heavy atoms of the polar head group with an equilibrated grafting cross-section of 53 Å^2/lipid ([3]) with the hydrophobic tails solvated in TIP3P water. The spatial domain for the molecular part is $45 \times 50 \times 50$ Å^3 and $780 \times 50 \times 50$ for the entire hybrid domain with periodic boundary condition in the x and y directions. We performed another set of simulations with a lower density monolayer with a cross-section of 69 Å^2/lipid.

This set-up has been also chosen so as to model experiments on slippage of water against hydrophobic layers [18]. In these experiments hydrophobic surfaces are prepared by coating a (otherwise hydrophilic) surfaces (such as mica) with a surfactant monolayer. The amount of slip over the surface is still a matter of controversy. Slip is re-

duced at high pressure, probably as water molecules are able to enter into the lipid layer. We defer such study for a future work and, here we present a more detailed analysis of our simulations on the water-lipid monolayer interaction mediated by sound. We show that water molecules carried by sound waves are able to enter well into the lipid layer.

In the subsequent analysis we first consider the reflection coefficient associated to different lipid monolayers. The reflection coefficient was calculated via the Riemann invariants associated with the propagating incoming and reflected waves. Riemann invariants decouple sound waves moving in positive and negative directions. The Riemann invariant associated with positive propagation is $f(x,t) = f(x - ct)$, while $g(x,t) = g(x + ct)$ corresponds to the negative one. The invariants are in fact related to the sound modes: $f = \delta p/(\rho_e c) - \delta u$ and $g = \delta p/(\rho_e c) + \delta u$. Here δp and δu denote the pressure and velocity variations due to the sound wave. As long as we are working near the thermodynamic (isothermal) equilibrium pressure variations are solely due to density variations, so that $\delta p = c^2 \delta \rho$. This permits us to evaluate the Riemann invariants as

$$f(x,t) = c\frac{\delta\rho}{\rho_e} + \delta u \tag{15}$$

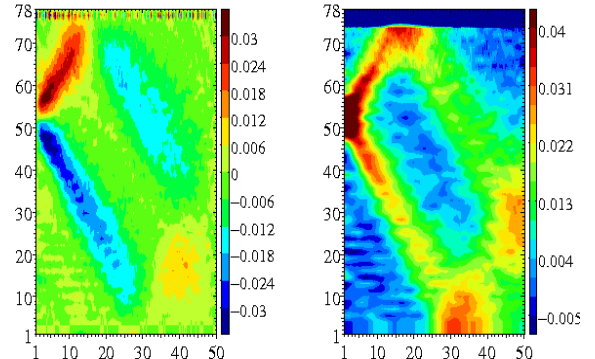$$g(x,t) = c\frac{\delta\rho}{\rho_e} - \delta u \tag{16}$$

FIG. 2: Spatio-temporal diagrams illustrating the isocontours of the longitudinal velocity (left) and density perturbation (right) of a sound wave propagating trought water and reflecting against a lipid layer. Abscissa are in picoseconds and coordinates in nm. The lipid layer is located at the top (it occupies about 2 nm). The total simulation time is 50 ps and the simulation box is 78 nm. In the present example the MD region has a rather large extent (18 nm).

Figure 2 shows the perturbation fields δu and $c\delta\rho/\rho_e$ for a simulation of a water based sound wave colliding with a lipid monolayer. In this example the MD region occupies 18 nm at the top of the Fig. 2 while at the

lower boundary a rigid, purely reflecting wall is imposed on the FH domain (the rest of the cases described in the foregoing discussion were performed with a much shorter MD domain of extent 4.5 nm , see Fig. 1). The resulting wave invariants f and g are shown in Fig. 3. The initial density perturbation produces two sound waves traveling in opposite directions, which in Fig. 3 are denoted as f_{in} and g_{in}. The wave moving in the positive x direction (f_{in}) collides with the lipid wall at about $t = 20$ps (a second f-wave originating from reflection of the g_{in}-wave against the lower boundary is also observed a later times). The first wave f_{in} is reflected against the upper wall and originates a reflected wave in the negative direction, denoted g_{out} (see Fig. 3). As long as $|f_{in}| = |g_{in}|$, a way to evaluate the reflection coefficient $r = g_{out}/f_{in}$, consists in evaluating the ratio $r(t) = \max[g_{out}]/\max[g_{in}]$, where $\max[f]$ denotes the maximum value obtained from the spatial dependence of the function f at a fixed time. Initially $g_{out} = 0$ and $r(t) = 0$. As shown in Fig. 4, after the incoming wave collides with the wall the value of $r(t)$ starts growing from zero and saturates at a constant value once the outgoing wave g_{out} completely leaves the wall region. The saturation value of $r(t)$ is the reflection coefficient.

Before presenting further results some technical details should be mentioned. Due to the fluctuating nature of the hydrodynamic fields the local maxima of f and g (where $df/dx = 0$) are not formally well defined. To solve this problem we performed 10 similar simulations using different random seeds in the FH field. From these simulations we evaluate the averaged f and g fields. Then, at each time, we filtered the high-wavenumber modes in the averaged f and g to extract the remaining noise. We used a simple Gaussian high-frequency filter G which, in the Fourier wavenumber k space, works as $\hat{f}(k,t) = f(k,t)G(k)$. This evaluation permits us to locate the maxima of f and g with better precision and accuracy.

Comparison of a lipid wall and a purely reflecting wall (PR). Figure 4 compares the instantaneous reflection coefficient $r(t)$ obtained for a sound wave colliding against a purely reflecting wall (solved by the FH code, without a molecular region) and similar sound waves impinging against a lipid layer (solved by hybrid MD). A first important difference is the delay that the lipid layer imposes on the outgoing wave. This is reflected in the lag of $r(t)$ with respect the PR wall, which is somewhat larger than 1 ps. This fact is due to the penetration of water inside the lipid layer. As shown in Fig. 5 (left) water molecules are able to penetrate into the lipid region a distance of about $\delta_i \sim 7\mathring{A}$. The delay time with respect the PR wall should then be $2\delta_i/c$ ps, where $c = 15\mathring{A}/ps$ is the sound velocity of water; an estimation which is in good agreement with the lag observed in Fig. 4. Second, the reflection coefficient of the lipid monolayer considered is close to one, albeit slightly smaller than the PR case. In fact, the lipid layer is not able to absorb much energy due to the close packing of the layer and the rigidity of the rela-
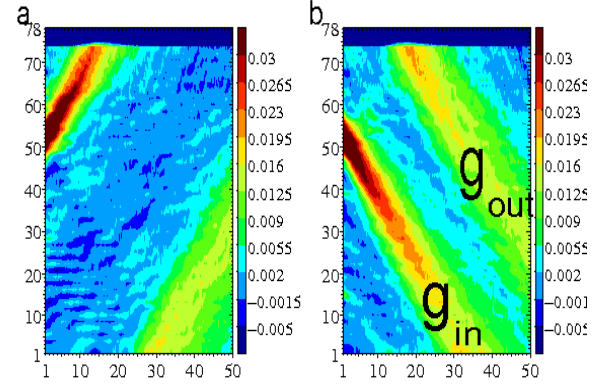

FIG. 3: Spatio-temporal diagrams for the Riemann invariants constructed from the fields shown in Fig. 2. Abscissa are in picoseconds and coordinates in nm. (a) Wave components in the positive direction $f(x,t)$ (the higher intensity wave at initial times is f_{in}) and (b) waves moving in the negative direction $g(x,t)$. In (b) we indicate the incoming wave g_{in} and the reflected wave g_{out} used to evaluate the reflection coefficient $r(t) = \max[g_{out}]/\max[g_{in}]$
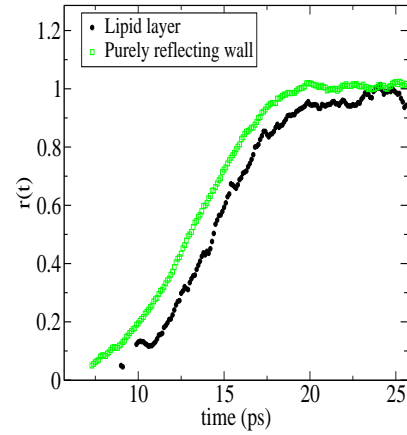

FIG. 4: The instantaneous reflection coefficient for the sound wave shown in Fig. 2, compared with the case of a similar water based sound wave colliding against a purely reflecting wall (solved via fluctuating hydrodynamics).

tively short molecules (the lipid molecule is about $L = 20$ nm long). However one should expect some deformation of the lipid tails which allows some water molecules to enter within the layer. The deformation of the lipid layer is shown in Fig. 5 (right) by plotting the evolution of the x-position of the end-atom of the lipid molecules, x_e^i, averaged over the whole layer; $\Delta X_e(t) \equiv X_e(t) - X_e(0)$, where $X_e = 1/N \sum_i x_e^i$. As shown in Fig. 5 (right) at the collision $\Delta X_e \simeq 0.5\mathring{A}$ so that the typical tilt angle of the lipid molecule is $\theta \sim (\Delta X_e/L)^{1/2}$ and the typical spacing in horizontal (normal-to-wall) direction is $2\theta L \sim 6\mathring{A}$. This is enough space for more than one water molecule
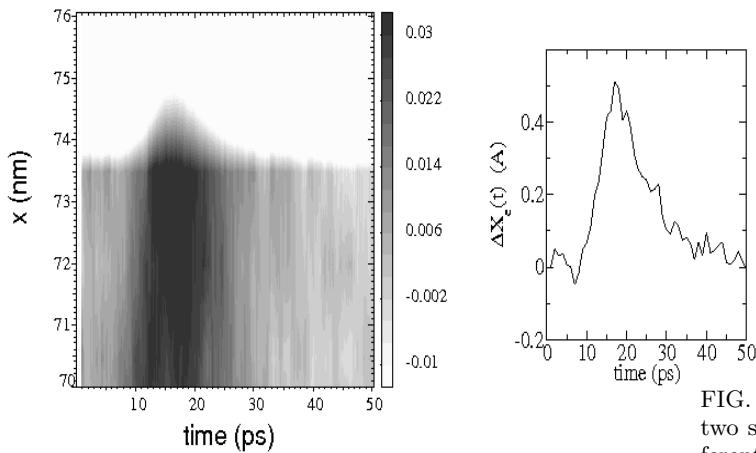
to be accommodated.

FIG. 5: (left) A close-up of the density field around the collision of the sound wave with the lipid layer. The lipid region is located at the top of the figure. Water is able to enter inside the lipid domain to a distance of about 7 to 10 $\mathring{A}$. (right) The average displacement of the end atoms of the lipid tails in the wave direction due to collision with the wave (see text).
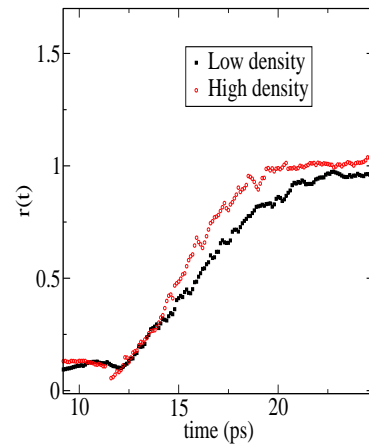

FIG. 6: The instantaneous reflection coefficient compared for two similar waves colliding against two lipid layers with different surface density. The larger density layer corresponds to 53 $\mathring{A}^2$/lipid and the lower density to 69 $\mathring{A}^2$/lipid.

Effect of the grafting density of the lipid layer. Figure 6 compares reflection coefficients $r(t)$ obtained for lower and higher density lipid layers. We find that the lower density layer is able to absorb some amount of energy from the wave, resulting in a lower saturation value of r. Also, the lag induced by the water molecules entering into the lipid layer is more pronounced. Lipids in the lower density layer have more space available in which to move and thus a larger entropy. This is reflected in a (more than twice) larger standard deviation of the lipid end-atom x-position (not shown). The maximum value of ΔX_e is, by contrast, only slightly larger in the lower density layer, indicating that most important difference between both layers is of entropic origin.

Effect of thermostat. In this discussion it is important to evaluate the effect of the thermostat intensity. We are actually working at wave numbers which are near the frontier between isothermal and adiabatic waves (see [3]). Hence, thermal effects should be limited, but appreciable. Figure 7 compares $r(t)$ for two simulations with different DPD thermostat intensities. The rate of heat removal by the hard thermostat is $\gamma = 102$g mol^{-1} ps^{-1}, while the soft thermostat removes heat at $\gamma = 2.05$g mol^{-1} ps^{-1}. The characteristic time of the soft thermostat (molecule mass/γ) is much longer than the sound time across the MD domain, thus one should not expect to have any influence on the dynamics. By contrast, the fast thermostat removes a significant amount of the energy produced by the wave around the lipid layer. This is reflected in a smaller value of $r(t)$ (i.e., the outgoing wave has lower energy) and also shown in Fig. 7b.

V. SUMMARY AND CONCLUSIONS

We have presented hybrid simulations of an ultrasound water wave colliding with a wall formed by a lipid monolayer. The hybrid method describes the region near the lipid layer, including the adjacent water molecules, via an atomistic description, while the bulk region of the solvent (water) is solved via fluctuating hydrodynamics. The coupling of both regions is performed by exchanging fluxes of mass and momentum. The analysis of the Riemann invariants of the incoming and reflected waves shows that the hybrid model is able to capture subtle differences arising from the molecular structure near an interface. These differences are highlighted by comparing the wave reflected by the lipid layer and a similar wave reflected by a purely reflecting wall. Once the sound wave impinges against the lipid wall, the lipid molecules tilt by a small angle, just enough to allow some water molecules to enter within the monolayer, a distance of about $7\mathring{A}$. The reflected wave thus is delayed by about 2 ps with respect to a wave colliding with a PR wall. The reflection coefficient measured far away from the wall (at the FH domain) is close to one for the lipid layer, however it is slightly smaller than the reflection obtained with a purely reflecting wall. The effect of different surface densities of the lipid molecules is also appreciable, although the lipid layers are quite rigid and do not absorb much kinetic energy from the wave. As a final remark we note that the MD part of the hybrid code allows to include any molecular structure in a standard way. Thus, the present hybrid method enables, for instance, the study of complex molecules or molecule's assemblies in aqueous solvent (such as proteins and membranes). One of the objectives of this paper is to encourage future works in this direction using this promising methodology.
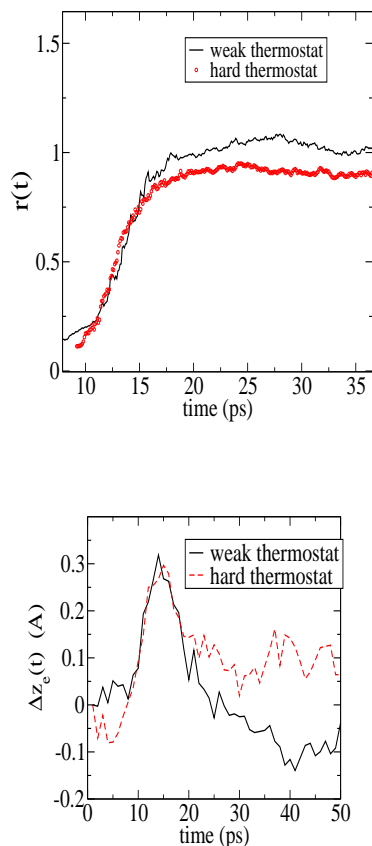
FIG. 7: (a) Comparison of the instantaneous reflection coefficients for two similar sound waves colliding with the larger surface density lipid layer (69 lipids/$\mathring{A}^2$) but with differing intensity of the DPD thermostat used in the MD region. The "hard" thermostat corresponds to $\gamma = 102$g mol^{-1}ps^{-1} and the "soft" one to $\gamma = 2.05$g mol^{-1}ps^{-1}; (b) The variation in time of the average position of the last lipid atom obtained with the hard and soft thermostat.

[1] G. De Fabritiis, M. Serrano, R. Delgado-Buscalioni, and P. V. Coveney, Phys. Rev. E **75**, 026307 (2007).

[2] L. D. Landau and E. M. Lifshitz, *Fluid Mechanics* (Pergamon Press, 1959).

[3] G. De Fabritiis, R. Delgado-Buscalioni, and P. Coveney, Phys. Rev. Lett **97**, 134501 (2006).

[4] J. Keizer, *Statistical thermodynamics of nonequilibrium processes* (Springer-Verlag, New York, 1987).

[5] M. Serrano and P. Español, Phys. Rev. E **64**, 046115 (2001).

[6] E. Flekkøy, P. Coveney, and G. De Fabritiis, Phys. Rev. E **62**, 2140 (2000).

[7] S. V. Patankar, *Numerical Heat Transfer and Fluid Flow* (Hemisphere, New York, 1980).

[8] L. Kalé, R. Skeel, M. Bhandarkar, R. Brunner, A. Gursoy, N. Krawetz, J. Phillips, A. Shinozaki, K. Varadarajan, and K. Schulten, J. Comp. Phys. **151**, 283 (1999).

[9] T. Soddemann, B. Dunweg, and K. Kremer, Phys. Rev. E **68**, 046702 (2003).

[10] P. Coveney, G. De Fabritiis, M. H. S. Pickles, and A. Porter, Comp. Phys. Commun. **175**, 389 (2006).

[11] P. Koumoutsakos, Ann. Rev. Fluid Mech. **37**, 457 (2005).

[12] E. G. Flekkoy, R. Delgado-Buscalioni, and P. V. Coveney, Phys. Rev. E **72**, 026703 (2005).

[13] M. Allen and D. Tildesley, *Computer Simulations of Liquids* (Oxford University Press, 1987).

[14] G. De Fabritiis, R. Delgado-Buscalioni, and P. V. Coveney, J. Chem. Phys. **121**, 12139 (2004).

[15] R. Delgado-Buscalioni and P. V. Coveney, J. Chem. Phys. **119**, 978 (2003).

[16] R. Delgado-Buscalioni and G. De Fabritiis, Phys. Rev. E **76**, 036709 (2007).

[17] E. Chacón, P. Tarazona, and J. Alejandre, J. Chem. Phys. **125**, 014709 (2006).

[18] C. Cottin-Bizonne, B. Cross, A. Stinberger, and E. Charlaix, Phys. Rev. Lett. **94**, 056102 (2005).